polymers

MDPI

Article

Unveiling the Role of Fluorination in Suppressing Dark Current and Enhancing Photocurrent to Enable Thick-Film Near-Infrared Organic Photodetectors

Yongqi Bai [1], Seon Lee Kwak [1], Jong-Woon Ha [2,*] and Do-Hoon Hwang [1,*]

[1] Department of Chemistry, Pusan National University, 2 Busandaehak-ro, Geumjeong-gu, Busan 46241, Republic of Korea; byongqi@163.com (Y.B.); gsun0331@naver.com (S.L.K.)
[2] Department of Materials Engineering and Convergence Technology, Gyeongsang National University, Jinju 52828, Republic of Korea
* Correspondence: hajw@gnu.ac.kr (J.-W.H.); dohoonhwang@pusan.ac.kr (D.-H.H.)

Abstract

Thick active layers are crucial for scalable production of organic photodetectors (OPDs). However, most OPDs with active layers thicker than 200 nm typically exhibit decreased photocurrents and responsivities due to exciton diffusion and prolonged charge transport pathways. To address these limitations, we designed and synthesized PFBDT-8ttTPD, a fluorinated polymer donor. The strategic incorporation of fluorine effectively enhanced the charge carrier mobility, enabling more efficient charge transport, even in thicker films. OPDs combining PFBDT−8ttTPD with IT−4F or Y6 non-fullerene acceptors showed a substantially lower dark current density (J_d) for active layer thicknesses of 250−450 nm. Notably, J_d in the IT-4F-based devices declined from 8.74×10^{-9} to 4.08×10^{-10} A cm^{-2} under a reverse bias of −2 V, resulting in a maximum specific detectivity of 3.78×10^{13} Jones. Meanwhile, Y6 integration provided near-infrared sensitivity, with the devices achieving responsivity above 0.48 A W^{-1} at 850 nm and detectivity over 10^{13} Jones up to 900 nm, supporting broadband imaging. Importantly, high-quality thick films (≥400 nm) free of pinholes or defects were fabricated, enabling scalable production without performance loss. This advancement ensures robust photodetection in thick uniform layers and marks a significant step toward the development of industrially viable OPDs.

Keywords: organic photodetectors; thick photoactive layer; high charge mobility; near-infrared; low dark current

check for updates

Academic Editor: Chi-Jung Chang

Received: 4 September 2025
Revised: 26 September 2025
Accepted: 27 September 2025
Published: 1 October 2025

Citation: Bai, Y.; Kwak, S.L.; Ha, J.-W.; Hwang, D.-H. Unveiling the Role of Fluorination in Suppressing Dark Current and Enhancing Photocurrent to Enable Thick-Film Near-Infrared Organic Photodetectors. *Polymers* **2025**, *17*, 2663. https://doi.org/10.3390/polym17192663

Copyright: © 2025 by the authors. Licensee MDPI, Basel, Switzerland. This article is an open access article distributed under the terms and conditions of the Creative Commons Attribution (CC BY) license (https://creativecommons.org/licenses/by/4.0/).

1. Introduction

In recent years, organic photodetectors (OPDs) have gained significant attention owing to their intrinsic advantages including flexibility, low−cost production via solution processing, controllable absorption wavelength, and higher intrinsic absorption coefficient compared with Si-based photodetectors [1–6]. The ability to tune the band gap of organic materials effectively is crucial for expanding the detection range to the near-infrared (NIR) region. This expansion will allow OPDs to be applied to diverse optoelectronic devices including image sensors, fingerprint scanners, biomedical sensors, and machine vision [7–10]. Recent development of non-fullerene acceptors (NFAs) has significantly extended the NIR photoresponse beyond 900 nm [11–15]. Yet, it remains very challenging to simultaneously achieve high detectivity (D^*) and low dark current density (J_d) at these

wavelengths, particularly when using scalable processes such as slot-die and roll-to-roll printing that often produce thick or non-uniform active layers.

Organic semiconductors typically possess short exciton diffusion lengths (generally <10 nm), requiring active layers thinner than 100 nm for effective exciton dissociation. However, practical printing processes often demand substantially thicker films to prevent pinholes and enhance uniformity [16–18]. As a result, films thicker than 200 nm exhibit considerable photocurrent losses in NFA-based OPDs due to low electron mobility of NFAs, which promotes recombination of excitons generated deep within the films [19]. Furthermore, while thicker films can suppress pinhole defects and ensure uniformity in practical printing, they also extend the charge−transport pathway and aggravate surface inhomogeneity, further degrading the photocurrent and D^* [20–23]. OPDs based on fullerene derivatives have higher electron mobilities (typically ~10^{-3} cm^2 V^{-1} s^{-1}) and therefore can partially mitigate these losses. For instance, Zeng et al. [24] reported a 400 nm-thick PNTT:$PC_{71}BM$ device with a J_d of 0.33 nA cm^{-2} under a reverse bias of –0.1 V and a specific D^* of 4×10^{13} Jones at 760 nm. Given that the absorption of PCBM sharply declines beyond ~550 nm and becomes negligible above ~700 nm, the response of the PNTT:$PC_{71}BM$ device at 760 nm relies exclusively on the donor polymer's absorption in the red region, highlighting the inherent limitations of fullerene acceptors for NIR detection [24]. Recent advances in NFAs have enabled OPDs with high photoresponse in the 800–1050 nm region [25–28]. Nevertheless, the intrinsically low electron mobilities of most NFAs lead to a rapid decline in photocurrent when the active layer is thicker than 200 nm. This is because excitons generated deep within the film recombine before extraction at the interface, owing to their limited diffusion and dissociation lengths [21,29]. Thus, the development of NFA-based devices that combine thick active layers (≥250 nm), high photocurrents, and low mboxemphJ_d remains an open and crucial challenge.

Owing to their high charge mobilities, thienopyrrolodione (TPD) −based polymer donors, notably PBDT−8ttTPD, have demonstrated the ability to sustain high D^* with 1 μm-thick films when blended with PCBM [30]. In this study, we applied strategic fluorination to the backbone of PBDT−8ttTPD to address the thickness-related performance loss in NFA-based OPDs. The rationale for this synthetic strategy is twofold. First, strong fluorine–fluorine (F−F) interactions promote coherent π–π stacking and improve the film uniformity. This leads to a reduction in energetic disorder and the suppression of both shallow and deep trap-state densities, as evidenced by prior research [31]. Secondly, the high electronegativity of fluorine effectively stabilizes frontier molecular orbitals of the polymer. This results in a downward shift of both the highest occupied molecular orbital (HOMO) and lowest unoccupied molecular orbital (LUMO) energy levels, importantly, without altering the overall bandgap [31]. This deeper energy alignment subsequently reduces the charge−injection rates, thereby minimizing the dark hole injection. Furthermore, the strong interactions between F atoms in adjacent molecules also contribute to tighter molecular packing within the film, which is directly correlated with a higher charge-carrier mobility. Collectively, these synergistic effects are expected to enable the fabrication of thick-film (~450 nm) NFA-based OPDs that minimize J_d while simultaneously achieving efficient photocurrent extraction.

2. Materials and Methods

2.1. Measurements

UV-Vis spectra were measured using a JASCO JP/V-570 instrument (Tokyo, Japan). The dark current and photocurrent curves of the OPDs were obtained using a Keithley 2635 B System SourceMeter (Tektronix, Solon, OH, USA). The devices were measured under an NIR LED light (Thorlabs M810L4) (tHORLABS, Dachau, Germany) in air. The light

intensity was adjusted using a standard photodiode power sensor (Thorlabs S120C). The external quantum efficiency (EQE) curves were measured using a McScience K3100 EQX system (Yeonggi-do, Republic of Korea). The EQE data were recorded as a function of wavelength in the range of 300–1100 nm using a xenon short-arc lamp as the light source, and calibration was performed using a Si photodiode. Grazing incident wide-angle X-ray scattering (GIWAXS) measurements were performed at beamline 3C in Pohang Accelerator Laboratory (Pohang in Republic of Korea).

2.2. Materials

All reagents for polymer synthesis and device fabrication were purchased from Alfa Aesar (Ward Hill, MA, USA), Aldrich (St. Louis, MI, USA), or TCI Korea (Seoul, Republic of Korea). IT-4F and Y6 were purchased from 1-Material. MoO_3 and Ag were purchased from iTASCO (Incheon, Republic of Korea).

2.3. Fabrication of OPDs

The OPDs were prepared with an inverted structure of indium tin oxide (ITO)/ZnO/active layer/MoO_3/Ag. The ZnO solution was prepared as reported previously [32]. Active layer solutions at various concentrations (20 to 40 mg mL^{-1}, polymer:NFAs = 1:1 *w*/*w*) were prepared using chloroform as the solvent and stirred overnight at 35 °C. The ITO substrates were sequentially cleaned in a hyperacoustic bath using detergent solution, distilled water, acetone, and then isopropanol for 10 min each. After treating the cleaned ITO substrates with UV-ozone plasma for 20 min, a ZnO layer was deposited on them according to the literature [32]. The active layer was coated in a glove box, and its thickness was controlled by changing the rotational speed and solution concentration. After drying the active layer, MoO_3 and Ag were thermally evaporated under a base pressure of 10^{-7} torr. The effective area of the active layer was 0.3 cm × 0.3 cm.

3. Results

Chemical structures of the donor polymer (PFBDT−8ttTPD) and two NFAs (IT−4F and Y6) are shown in Figure 1a. PFBDT−8ttTPD was synthesized via a Stille polycondensation reaction using $Pd(PPh_3)_4$ as the catalyst (Scheme S1). The resulting polymer exhibits excellent solubility (>20 mg mL^{-1}) in common chlorinated solvents such as chloroform, chlorobenzene, and *o*-dichlorobenzene. As shown in Figure 1b, the UV-Vis absorption spectra of neat PFBDT−8ttTPD films reveal an absorption onset at app-roximately 650 nm, corresponding to an optical bandgap of approximately 1.9 eV. This absorption profile effectively complements those of both IT−4F and Y6. Notably, the PFBDT-8ttTPD:Y6 blend exhibited extended absorption into the NIR region, reaching approximately 900 nm, whereas the absorption of the PFBDT−8ttTPD:IT−4F blend was limited to approximately 800 nm (Figure 1c). These findings suggest that the PFBDT-8ttTPD:Y6 system holds significant promise for achieving photodetection in the high NIR range. Cyclic voltammetry was employed to determine the energy levels of all photoactive materials. Figure 1d shows the resulting cascade energy level alignment between PFBDT-8ttTPD and both NFAs, indicating efficient pathways for charge separation and collection.

Inverted OPDs utilizing PFBDT−8ttTPD as the polymer donor were systematically evaluated for their photodetection performance. These OPDs have an architecture of ITO/ZnO/active layer/MoO_3/Ag (as shown in Figure 2a), employing a donor:acceptor ratio of 1:1 (*w*/*w*) without additives and pre−annealed for 10 min at 90 °C. The active layer thickness was varied from 200 to 450 nm to investigate its impact on the device metrics; the details are summarized in Tables S1 and S2. The optimal device performance was observed at 450 nm for PFBDT-8ttTPD:IT−4F and 420 nm for PFBDT−8ttTPD:Y6. When the thickness increased to these

optimal values, there was a notable reduction in J_d under a reverse bias of −2 V. For the IT−4F devices, J_d decreased significantly from 8.74×10^{-9} at 250 nm to 4.08×10^{-10} A cm^{-2} at 450 nm. In contrast, the Y6 devices reached a plateau in J_d at approximately 2.03×10^{-9} A cm^{-2} beyond a thickness of 420 nm. A substantial reduction in the J_d of OPDs was achieved by increasing the photoactive layer thickness [32,33]. Furthermore, the Y6-based OPDs exhibited a slightly higher J_d than their IT−4F counterparts. This difference is likely due to the lower effective bandgap of Y6 and the potentially higher hole-injection rate from the MoO_3/Ag interface into Y6. Despite the inherently weaker internal electric field in thicker films, which could potentially suppress the photocurrent density (J_{ph}), the measured J_{ph} remained high for all thicknesses, proving the compensatory role of the fluorinated polymer donor with excellent charge mobility. Indeed, the high charge carrier mobilities of PFBDT−8ttTPD ($\mu_h \approx 3.3 \times 10^{-4}$ cm^2 V^{-1} s^{-1} and $\mu_E \approx 2.3 \times 10^{-4}$ cm^2 V^{-1} s^{-1} [31]) are pivotal in sustaining efficient photocurrent extraction across the investigated thickness range (Figure 2b). The EQE spectra under −2 V bias were measured to determine the spectral responsivity (R = EQE × λ/1240). The PFBDT-8ttTPD:Y6 devices consistently outperformed the IT-4F devices in the visible-to-NIR spectrum (Figure 2c). The maximum R values were 0.43 A W^{-1} at 760 nm for PFBDT−8ttTPD:IT-4F and 0.48 A W^{-1} at 850 nm for PFBDT−8ttTPD:Y6. Remarkably, the PFBDT−8ttTPD:Y6 devices maintained a responsivity greater than 0.33 A W^{-1} even at 900 nm, highlighting their superior NIR photodetection performance. The specific D^*, which was estimated using the equation $D^* = R/(2qJ_d)^{1/2}$, reached an impressive value of 3.78×10^{13} Jones at 780 nm for PFBDT-8ttTPD:IT−4F. As shown in Figure 2d, the Y6−based OPDs also demonstrated competitive specific D^* exceeding 1.89×10^{13} Jones at 850 nm and 1.29×10^{13} Jones at 900 nm, further confirming sensitivity in the NIR region (Table 1). Although the Y6−based OPDs exhibited a relatively higher J_d (approximately $\times 10^{-9}$ A cm^{-2}) compared to PFBDT−8ttTPD:IT−4F, their overall performance remained competitive. Notably, these OPDs demonstrated effective photoresponse in the NIR region, underscoring their potentials for specific NIR applications. As presented in Table S1, our NFA-based OPDs deliver outstanding performance even at the thick photoactive layer, outperforming most reported NIR OPDs.

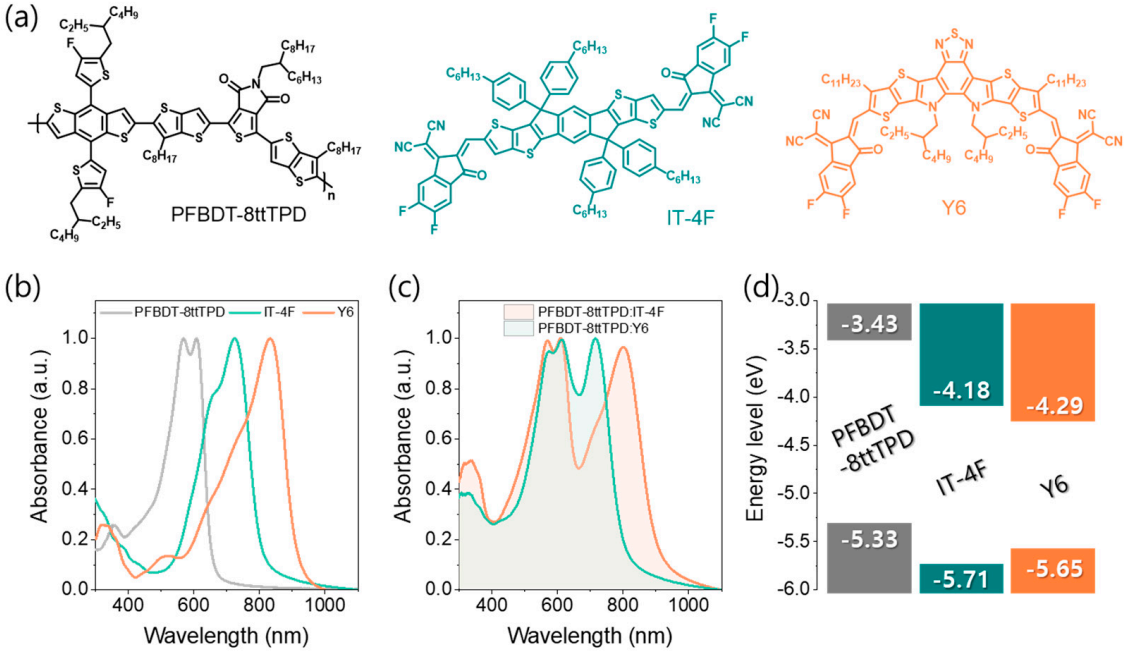


Figure 1. (**a**) Chemical structures of PFBDT−8ttTPD, IT−4F, and Y6. (**b**) Normalized UV−Vis absorption spectra of neat PFBDT−8ttTPD, IT−4F, and Y6 films. (**c**) Normalized UV−Vis absorption spectra of blend films. (**d**) Energy-level diagram of PFBDT−8ttTPD, IT−4F, and Y6 as determined by cyclic voltammetry.

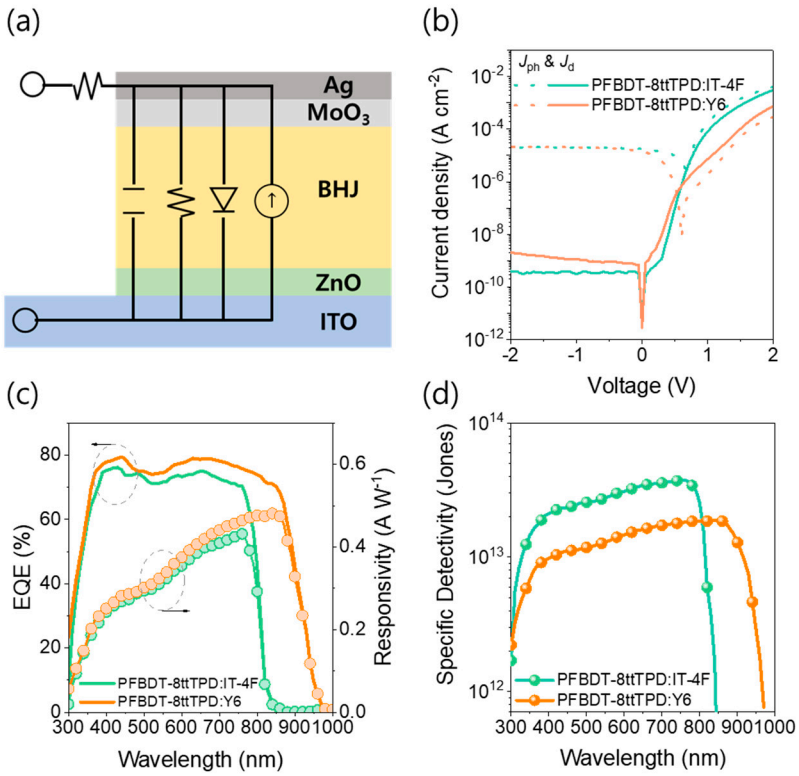


Figure 2. (**a**) Schematic illustration of the inverted configuration for OPDs. (**b**) Current−voltage characteristics measured in the dark and under standard solar illumination for PFBDT−8ttTPD:IT−4F (thickness: 450 nm) and PFBDT−8ttTPD:Y6 (420 nm). (**c**) External quantum efficiency and spectral responsivity curves for PFBDT−8ttTPD:IT−4F (450 nm) and PFBDT−8ttTPD:Y6 (420 nm). (**d**) Wavelength−dependent specific detectivity for PFBDT−8ttTPD:IT−4F (450 nm) and PFBDT−8ttTPD:Y6 (420 nm).

Table 1. Summary of the thickness-dependent performance for PFBDT−8ttPTD:NFAs under a reverse bias of –2.0 V.

	Thickness [nm]	J_d [A cm^{-2}]	J_{ph} [A cm^{-2}] [c]	R [A W^{-1}]	D^* [Jones]
PFDBT−8ttTPD :IT−4F [a]	250	8.74×10^{-9}	2.18×10^{-5}	0.43	2.52×10^{12}
	350	7.43×10^{-10}	2.00×10^{-5}	0.43	2.77×10^{13}
	450	4.08×10^{-10}	2.06×10^{-5}	0.43	3.78×10^{13}
PFBDT−8ttTPD :Y6 [b]	250	4.79×10^{-8}	2.12×10^{-5}	0.44	3.60×10^{12}
	450	2.03×10^{-9}	1.86×10^{-5}	0.48	1.89×10^{13}

[a] Responsivity and detectivity measured for PFBDT-8ttTPD:IT-4F (@760 nm). [b] Responsivity and detectivity measured for PFBDT-8ttTPD:Y6 (@850 nm). [c] Photocurrent density measured under LED illumination (@810 nm, 55.66 μW·cm^{-2}).

Figure 3a shows the atomic force microscopy (AFM) topographies of the PFBDT−8ttTPD:IT−4F and PFBDT−8ttTPD:Y6 blend films with different thicknesses. Both systems maintained exceptionally low root−mean−square (RMS) roughness values (<1.1 nm) even as the film thickness increased. Specifically, the RMS roughness for the IT−4F blend increased from 0.78 to 0.82 nm, while for the Y6 blend it rose from 0.74 to 1.02 nm as the film thickness increased from 250 to 420 nm. Despite these slight increases in the RMS roughness, the film surfaces stayed exceptionally smooth and devoid of pinholes or defects, which is crucial for minimizing J_d in thick−film OPDs. Figure 3b,c present the two−dimensional grazing incidence wide−angle X−ray diffraction (2D-GIWAXS) images and the corresponding line−cut profiles along the in−plane (IP) and out−of−plane (OOP) directions. Neat PFBDT-8ttTPD exhibits lamellar stacking at

q ≈ 0.28 Å^{-1} (d ≈ 22.4 Å and crystal coherence length (L_c) ≈ 78.5 Å) and π−π stacking at q ≈ 1.64 Å^{-1} (d ≈ 3.83 Å and L_c ≈ 18.5 Å), consistent with a dominant face-on orientation. Upon blending with IT−4F, the π−π stacking distance contracts to ~3.63 Å, and L_c increases to ~31.4 Å, reflecting tighter molecular packing and larger crystalline domains. In contrast, the Y6 blend maintains a π−π stacking distance (~3.78 Å) similar to that of neat PFBDT−8ttTPD, but shows a reduced coherence length (~18.0 Å), indicative of smaller domain sizes. Based on the GIWAXS analysis, the PFBDT−8ttTPD:IT−4F blend exhibits a shorter π−π stacking distance and a substantially longer coherence length, suggesting the preservation of long−range molecular order even in thick films. This dense crystalline packing shortens the vertical charge−transport pathways and suppresses trap density, thereby enabling the simultaneous minimization of J_d and enhancement of J_{ph} in PFBDT−8ttTPD:IT−4F. The PFBDT−8ttTPD:Y6 blend maintains a comparable π−π spacing but displays a shorter L_c, indicating smaller crystalline domains. Although this may increase carrier recombination at the domain boundaries, the Y6-based films capitalizes on their intrinsic NIR absorption to sustain photocurrent response up to 900 nm, demonstrating exceptional deep−NIR sensitivity. Ultimately, these GIWAXS−derived insights into the molecular ordering and domain size help explain how low J_d and high D^* can be simultaneously achieved in thick-film NFA−based OPDs.

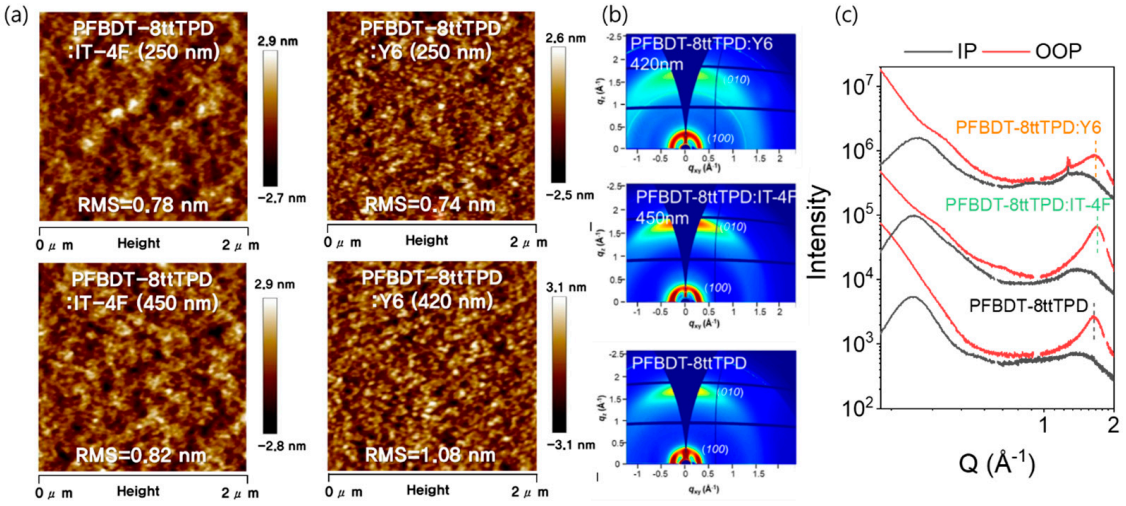


Figure 3. (**a**) AFM images of PFBDT-8ttTPD:NFAs at different active layer thicknesses. (**b**) 2D−GIWAXS images and (**c**) corresponding line−cut profile for neat PFBDT−8ttTPD, PFBDT−8ttTPD:IT−4F (450 nm), and PFBDT−8ttTPD:Y6 (420 nm).

The current densities of the PFBDT−8ttTPD-based OPDs were measured as a function of LED illumination intensity (I_a) in order to probe both bimolecular and trap-assisted recombinations in these devices (Figure 4a). According to the power−law relationship (current density ∝ $I_a{}^{\alpha}$), an α value approaching unity indicates effective suppression of bimolecular recombination pathways [28,29]. Indeed, both OPD devices exhibit α > 0.98, confirming minimal bimolecular recombination losses. Figure 4b (V_{OC} vs. ln(I_a)) yields the apparent ideality factors of 1.31 kT/q for PFBDT−8ttTPD:IT-4F and 1.52 kT/q for PFBDT−8ttTPD:Y6. An ideality factor (n) exceeding unity signifies trap−assisted recombination. Accordingly, the higher n value in the Y6−based devices compared to the IT−4F−based ones confirms more pronounced trap−mediated losses in the former. These recombination dynamic behaviors align with the GIWAXS observations, because the larger crystalline domains in the PFBDT−8ttTPD:IT−4F films reduce the trap site density in thick active layers.

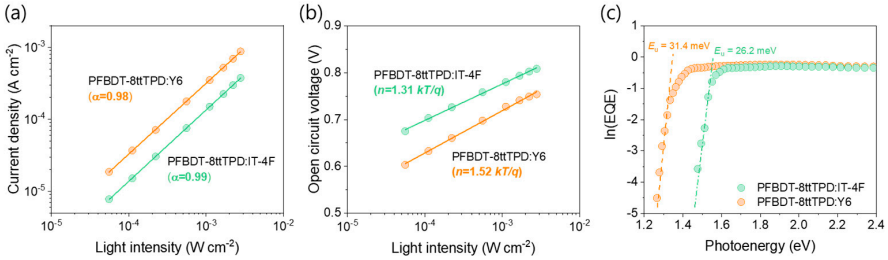


Figure 4. Variation in (**a**) short−circuit current density and (**b**) open−circuit voltage as a function of light intensity for PFBDT-8ttTPD:NFAs. (**c**) Extraction of Urbach energy from ln(EQE) in the long-wavelength edge for PFBDT-8ttTPD:NFAs.

Subsequently, energetic disorder in the photoactive layers was quantified using a sensitive EQE-based analysis. It involved determining the Urbach energy (E_U), which characterizes the extent of band−tail disorder [34,35] and was extracted from the sub-bandgap slope of ln(EQE) vs. photon energy ($h\nu$) using the relation $\ln(EQE) = c + h\nu/E_u$ [36]. As depicted in Figure 4c, the exponential rise of the absorption edge below the bandgap, commonly known as the Urbach tail, directly correlates with non−radiative recombination mediated by energetic disorder. The extracted E_U values are approximately 26.2 meV for PFBDT−8ttTPD:IT−4F and 31.4 meV for PFBDT−8ttTPD:Y6 devices. The reduced disorder in the PFBDT−8ttTPD:IT−4F blend is consistent with its larger coherence lengths, as observed using GIWAXS, suggesting more ordered and larger domains that effectively reduce trap-assisted recombination and contribute to the observed suppression of J_d.

The linear dynamic range (LDR) is defined as $20\log(J_{max}/J_{min})$ within the linear photocurrent regime, where J_{max} is the maximum J_{ph} and J_{min} the dark current density. LDR reaches 127 dB for PFBDT-8ttTPD:IT-4F under a reverse bias of −2.0 V, surpassing that of commercial silicon OPDs (120 dB) [37–39], and PFBDT-8ttTPD:Y6 also has a high LDR at ~112 dB. These exceptional LDR values directly reflect the pronounced trap-state suppression and reduced energetic disorder achieved via fluorination. The dynamic response was further characterized using the −3 dB cutoff frequency (f-3dB), the frequency at which the photocurrent responsivity falls to $1/\sqrt{2}$ of its low-frequency value under the same bias. PFBDT-8ttTPD:IT-4F exhibits an f-3dB of 52.8 kHz, compared to 43.6 kHz for the Y6-based OPD (Figure 5a), and both rates meet the requirements for video−rate imaging and medical monitoring applications [40]. Transient photovoltage measurements under 0.5 s square−wave illumination (Figure 5b,c) yielded a rise time (T_r, from 10% to 90%) of 8.0 µs and a fall time (T_f, from 90% to 10%) of 10.1 µs for PFBDT-8ttTPD:IT-4F. In contrast, the Y6 devices exhibited comparatively longer response times ($T_r \approx 15.0$ µs and $T_f \approx 19.2$ µs) [41]. The relatively faster T_r of PFBDT-8ttTPD:IT-4F correlates with its faster charge−carrier mobility, whereas the shorter T_d arises from its lower dark-current level, together highlighting the advantages of fluorination for high-speed, low-noise detection using thick-film OPDs.

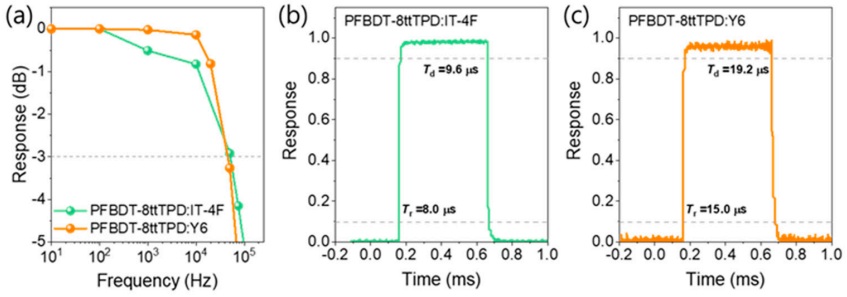


Figure 5. (**a**) Characterization of the dynamic behavior of both fabricated OPDs at −3dB cutoff frequencies. Transient photovoltage characteristics of (**b**) PFBDT−8ttTPD:IT−4F and (**c**) PFBDT−8ttTPD:Y6.

4. Conclusions

In conclusion, strategic fluorination in the PFBDT−8ttTPD backbone effectively overcomes thickness-induced performance losses in NFA-based OPDs. Our findings demonstrate that the thick active layers maintain ultra−smooth and pinhole-free morphologies, while GIWAXS analysis reveals enhanced π−π stacking and sustained long−range molecular order. The excellent charge-carrier mobilities inherent to the fluorinated polymer compensate for the weaker internal field in thicker films, thereby enabling efficient photocurrent extraction. Consequently, a drastic reduction in the dark current density is achieved, leading to outstanding detectivity and responsivity across the NIR spectrum. Thus, this fluorination approach enables the fabrication of high−performance OPDs with thick active layers via scalable solution processing, offering a promising route for robust imaging applications. Future studies will focus on molecular design strategies to broaden the spectral sensitivity and enhance the long-term operational stability.

Supplementary Materials: The following supporting information can be downloaded at: https://www.mdpi.com/article/10.3390/polym17192663/s1, Scheme S1: The synthetic route of PFBDT−8ttTPD; Table S1: Comparison of the photodetection performance in the literature.

Author Contributions: Conceptualization, Y.B. and D.-H.H.; methodology, Y.B.; investigation, Y.B.; writing—original draft preparation, Y.B.; writing—review and editing, S.L.K., J.-W.H., and D.-H.H.; supervision, J.-W.H. and D.-H.H. All authors have read and agreed to the published version of the manuscript.

Funding: This work was supported by a National Research Foundation of Korea (NRF) grant funded by the Korean government (MSIT) (RS-2023-00280495) and the New Faculty Research Support Grant from Gyeongsang National University in 2025 (GNU-NFRSG-0008*).

Institutional Review Board Statement: Not applicable.

Data Availability Statement: The original contributions presented in this study are included in the article and Supplementary Material. Further inquiries can be directed to the corresponding authors.

Conflicts of Interest: The authors declare no conflicts of interest.

References

1. Azzellino, G.; Grimoldi, A.; Binda, M.; Caironi, M.; Natali, D.; Sampietro, M. Fully Inkjet-Printed Organic Photodetectors with High Quantum Yield. *Adv. Mater.* **2013**, *25*, 6829–6833. [CrossRef]
2. Pace, G.; Grimoldi, A.; Natali, D.; Sampietro, M.; Coughlin, J.E.; Bazan, G.C.; Caironi, M. All-Organic and Fully-Printed Semitransparent Photodetectors Based on Narrow Bandgap Conjugated Molecules. *Adv. Mater.* **2014**, *26*, 6773–6777. [CrossRef]
3. Pierre, A.; Deckman, I.; Lechêne, P.B.; Arias, A.C. High Detectivity All-Printed Organic Photodiodes. *Adv. Mater.* **2015**, *27*, 6411–6417. [CrossRef]
4. Simone, G.; Dyson, M.J.; Meskers, S.C.J.; Janssen, R.A.J.; Gelinck, G.H. Organic Photodetectors and their Application in Large Area and Flexible Image Sensors: The Role of Dark Current. *Adv. Funct. Mater.* **2020**, *30*, 1904205. [CrossRef]
5. Wu, Y.-L.; Fukuda, K.; Yokota, T.; Someya, T. A Highly Responsive Organic Image Sensor Based on a Two-Terminal Organic Photodetector with Photomultiplication. *Adv. Mater.* **2019**, *31*, 1903687. [CrossRef]
6. Yamamoto, K.; Nakajima, A.; Yoshimi, M.; Sawada, T.; Fukuda, S.; Suezaki, T.; Ichikawa, M.; Koi, Y.; Goto, M.; Meguro, T.; et al. A high efficiency thin film silicon solar cell and module. *Sol. Energy* **2004**, *77*, 939–949. [CrossRef]
7. Armin, A.; Hambsch, M.; Kim, I.K.; Burn, P.L.; Meredith, P.; Namdas, E.B. Thick junction broadband organic photodiodes. *Laser Photonics Rev.* **2014**, *8*, 924–932. [CrossRef]
8. Baierl, D.; Pancheri, L.; Schmidt, M.; Stoppa, D.; Betta, G.-F.D.; Scarpa, G.; Lugli, P. A hybrid CMOS-imager with a solution-processable polymer as photoactive layer. *Nat. Commun.* **2012**, *3*, 1175. [CrossRef] [PubMed]
9. Liu, Z.; Parvez, K.; Li, R.; Dong, R.; Feng, X.; Müllen, K. Transparent Conductive Electrodes from Graphene/PEDOT:PSS Hybrid Inks for Ultrathin Organic Photodetectors. *Adv. Mater.* **2015**, *27*, 669–675. [CrossRef] [PubMed]
10. Simone, G.; Di Carlo Rasi, D.; de Vries, X.; Heintges, G.H.L.; Meskers, S.C.J.; Janssen, R.A.J.; Gelinck, G.H. Near-Infrared Tandem Organic Photodiodes for Future Application in Artificial Retinal Implants. *Adv. Mater.* **2018**, *30*, 1804678. [CrossRef] [PubMed]

11. Deng, S.; Zhang, L.; Zheng, J.; Li, J.; Lei, S.; Wu, Z.; Yang, D.; Ma, D.; Chen, J. A Simple Fused-Ring Acceptor toward High-Sensitivity Binary Near-Infrared Photodetector. *Adv. Opt. Mater.* **2022**, *10*, 2200371. [CrossRef]
12. Ha, J.-W.; Eun, H.J.; Park, B.; Ahn, H.; Hwang, D.R.; Shim, Y.S.; Heo, J.; Lee, C.; Yoon, S.C.; Kim, J.H.; et al. Effect of Cyano Substitution on Non-Fullerene Acceptor for Near-Infrared Organic Photodetectors above 1000 nm. *Adv. Funct. Mater.* **2023**, *33*, 2211486. [CrossRef]
13. Huang, J.; Lee, J.; Vollbrecht, J.; Brus, V.V.; Dixon, A.L.; Cao, D.X.; Zhu, Z.; Du, Z.; Wang, H.; Cho, K.; et al. A High-Performance Solution-Processed Organic Photodetector for Near-Infrared Sensing. *Adv. Mater.* **2020**, *32*, 1906027. [CrossRef] [PubMed]
14. Yang, M.; Yin, B.; Hu, G.; Cao, Y.; Lu, S.; Chen, Y.; He, Y.; Yang, X.; Huang, B.; Li, J.; et al. Sensitive short-wavelength infrared photodetection with a quinoidal ultralow band-gap n-type organic semiconductor. *Chem* **2024**, *10*, 1425–1444. [CrossRef]
15. Yin, B.; Zhou, X.; Li, Y.; Hu, G.; Wei, W.; Yang, M.; Jeong, S.; Deng, W.; Wu, B.; Cao, Y.; et al. Sensitive Organic Photodetectors With Spectral Response up to 1.3 μm Using a Quinoidal Molecular Semiconductor. *Adv. Mater.* **2024**, *36*, 2310811. [CrossRef]
16. Mikhnenko, O.V.; Blom, P.W.M.; Nguyen, T.-Q. Exciton diffusion in organic semiconductors. *Energy Environ. Sci.* **2015**, *8*, 1867–1888. [CrossRef]
17. Firdaus, Y.; Le Corre, V.M.; Karuthedath, S.; Liu, W.; Markina, A.; Huang, W.; Chattopadhyay, S.; Nahid, M.M.; Nugraha, M.I.; Lin, Y.; et al. Long-range exciton diffusion in molecular non-fullerene acceptors. *Nat. Commun.* **2020**, *11*, 5220. [CrossRef]
18. Stübinger, T.; Brütting, W. Exciton diffusion and optical interference in organic donor–acceptor photovoltaic cells. *J. Appl. Phys.* **2001**, *90*, 3632–3641. [CrossRef]
19. Najafov, H.; Lee, B.; Zhou, Q.; Feldman, L.C.; Podzorov, V. Observation of long-range exciton diffusion in highly ordered organic semiconductors. *Nat. Mater.* **2010**, *9*, 938–943. [CrossRef]
20. Li, L.; Zhang, F.; Wang, W.; An, Q.; Wang, J.; Sun, Q.; Zhang, M. Trap-Assisted Photomultiplication Polymer Photodetectors Obtaining an External Quantum Efficiency of 37 500%. *ACS Appl. Mater. Interfaces* **2015**, *7*, 5890–5897. [CrossRef]
21. Zeiske, S.; Sandberg, O.J.; Zarrabi, N.; Li, W.; Meredith, P.; Armin, A. Direct observation of trap-assisted recombination in organic photovoltaic devices. *Nat. Commun.* **2021**, *12*, 3603. [CrossRef]
22. Ma, X.; Janssen, R.A.J.; Gelinck, G.H. Trap-Assisted Charge Generation and Recombination in State-of-the-Art Organic Photodetectors. *Adv. Mater. Technol.* **2023**, *8*, 2300234. [CrossRef]
23. Sandberg, O.J.; Kaiser, C.; Zeiske, S.; Zarrabi, N.; Gielen, S.; Maes, W.; Vandewal, K.; Meredith, P.; Armin, A. Mid-gap trap state-mediated dark current in organic photodiodes. *Nat. Photonics* **2023**, *17*, 368–374. [CrossRef]
24. Zeng, Z.; Zhong, Z.; Zhong, W.; Zhang, J.; Ying, L.; Yu, G.; Huang, F.; Cao, Y. High-detectivity organic photodetectors based on a thick-film photoactive layer using a conjugated polymer containing a naphtho[1,2-c:5,6-c]bis[1,2,5]thiadiazole unit. *J. Mater. Chem. C* **2019**, *7*, 6070–6076. [CrossRef]
25. Zhang, Y.; Yu, Y.; Liu, X.; Miao, J.; Han, Y.; Liu, J.; Wang, L. An n-Type All-Fused-Ring Molecule with Photoresponse to 1000 nm for Highly Sensitive Near-Infrared Photodetector. *Adv. Mater.* **2023**, *35*, 2211714. [CrossRef]
26. Wang, W.; Miao, X.; Cai, G.; Ding, L.; Li, Y.; Li, T.; Zhu, Y.; Tao, L.; Jia, Y.; Liang, Y.; et al. Enhancing Transition Dipole Moments of Heterocyclic Semiconductors via Rational Nitrogen-Substitution for Sensitive Near Infrared Detection. *Adv. Mater.* **2022**, *34*, 2201600. [CrossRef]
27. Lee, J.; Ko, S.-J.; Lee, H.; Huang, J.; Zhu, Z.; Seifrid, M.; Vollbrecht, J.; Brus, V.V.; Karki, A.; Wang, H.; et al. Side-Chain Engineering of Nonfullerene Acceptors for Near-Infrared Organic Photodetectors and Photovoltaics. *ACS Energy Lett.* **2019**, *4*, 1401–1409. [CrossRef]
28. Lee, U.-H.; Park, B.; Rhee, S.; Ha, J.-W.; Whang, D.R.; Eun, H.J.; Kim, J.H.; Shim, Y.; Heo, J.; Lee, C.; et al. Achieving Highly Sensitive Near-Infrared Organic Photodetectors using Asymmetric Non-Fullerene Acceptor. *Adv. Opt. Mater.* **2023**, *11*, 2300312. [CrossRef]
29. Babics, M.; Bristow, H.; Zhang, W.; Wadsworth, A.; Neophytou, M.; Gasparini, N.; McCulloch, I. Non-fullerene-based organic photodetectors for infrared communication. *J. Mater. Chem. C* **2021**, *9*, 2375–2380. [CrossRef]
30. Park, J.B.; Ha, J.-W.; Yoon, S.C.; Lee, C.; Jung, I.H.; Hwang, D.-H. Visible-Light-Responsive High-Detectivity Organic Photodetectors with a 1 μm Thick Active Layer. *ACS Appl. Mater. Interfaces* **2018**, *10*, 38294–38301. [CrossRef]
31. Ha, J.-W.; Song, C.E.; Kim, H.S.; Ryu, D.H.; Shin, W.S.; Hwang, D.-H. Highly Efficient and Photostable Ternary Organic Solar Cells Enabled by the Combination of Non-Fullerene and Fullerene Acceptors with Thienopyrrolodione-based Polymer Donors. *ACS Appl. Mater. Interfaces* **2020**, *12*, 51699–51708. [CrossRef]
32. Sun, Y.; Seo, J.H.; Takacs, C.J.; Seifter, J.; Heeger, A.J. Inverted polymer solar cells integrated with a low-temperature-annealed sol-gel-derived ZnO Film as an electron transport layer. *Adv. Mater.* **2011**, *23*, 1679. [CrossRef]
33. Ha, J.-W.; Eom, S.H.; Cha, B.K.; Song, S.; Eun, H.J.; Kim, J.H.; Park, J.M.; Kim, B.; Park, B.; Ko, S.-J.; et al. Organic X-Ray Image Sensors Using a Medium Bandgap Polymer Donor with Low Dark Current. *Energy Environ. Mater.* **2024**, *7*, e12750. [CrossRef]
34. Liu, S.; Yuan, J.; Deng, W.; Luo, M.; Xie, Y.; Liang, Q.; Zou, Y.; He, Z.; Wu, H.; Cao, Y. High-efficiency organic solar cells with low non-radiative recombination loss and low energetic disorder. *Nat. Photonics* **2020**, *14*, 300–305. [CrossRef]

35. Venkateshvaran, D.; Nikolka, M.; Sadhanala, A.; Lemaur, V.; Zelazny, M.; Kepa, M.; Hurhangee, M.; Kronemeijer, A.J.; Pecunia, V.; Nasrallah, I.; et al. Approaching disorder-free transport in high-mobility conjugated polymers. *Nature* **2014**, *515*, 384–388. [CrossRef] [PubMed]
36. Chantana, J.; Kawano, Y.; Nishimura, T.; Minemoto, T. Urbach energy of Cu(In,Ga)Se_2 and Cu(In,Ga)$(S,Se)_2$ absorbers prepared by various methods: Indicator of their quality. Mater. *Today Commun.* **2019**, *21*, 100652. [CrossRef]
37. Kielar, M.; Dhez, O.; Pecastaings, G.; Curutchet, A.; Hirsch, L. Long-Term Stable Organic Photodetectors with Ultra Low Dark Currents for High Detectivity Applications. *Sci. Rep.* **2016**, *6*, 39201. [CrossRef]
38. Jang, W.; Rasool, S.; Kim, B.G.; Kim, J.; Yoon, J.; Manzhos, S.; Lee, H.K.; Jeon, I.; Wang, D.H. Superior Noise Suppression, Response Time, and Device Stability of Non-Fullerene System over Fullerene Counterpart in Organic Photodiode. *Adv. Funct. Mater.* **2020**, *30*, 2001402. [CrossRef]
39. Leem, D.-S.; Lee, K.-H.; Li, N.; Park, B.W.; Choi, T.; Ro, T.; Kwon, O.K.; Kwon, Y.-N.; Ng, T.N.; Kim, S. Highly Responsive and Thermally Reliable Near-Infrared Organic Photodiodes Utilizing Naphthalocyanine Molecules Tuned with Axial Ligands. *Adv. Opt. Mater.* **2021**, *9*, 2001682. [CrossRef]
40. Deckman, I.; Lechêne, P.B.; Pierre, A.; Arias, A.C. All-printed full-color pixel organic photodiode array with a single active layer. *Org. Elerctron.* **2018**, *56*, 139–145. [CrossRef]
41. Jeong, W.; Kang, J.; Lim, S.Y.; Ahn, H.; Kim, H.M.; Won, J.H.; Jung, I.H. Spontaneously Induced Hierarchical Structure by Surface Energy in Novel Conjugated Polymer-Based Ultrafast-Response Organic Photodetectors. *Adv. Opt. Mater.* **2022**, *10*, 2102607. [CrossRef]

Disclaimer/Publisher's Note: The statements, opinions and data contained in all publications are solely those of the individual author(s) and contributor(s) and not of MDPI and/or the editor(s). MDPI and/or the editor(s) disclaim responsibility for any injury to people or property resulting from any ideas, methods, instructions or products referred to in the content.